Q-factor Bounds for Microstrip Patch Antennas

Nel, Ben; Skrivervik, Anja; Gustafsson, Mats

Published in:
IEEE Transactions on Antennas and Propagation

DOI:
10.1109/TAP.2023.3243726

2023

Document Version:
Early version, also known as pre-print

CODEN:LUTEDX/(TEAT-7275)/1-24/(2023)

Q-factor Bounds for Microstrip Patch Antennas

Ben A.P. Nel, Anja K. Skrivervik, and Mats Gustafsson

Electromagnetic Theory
Department of Electrical and Information Technology
Lund University
Sweden

(TEAT-7275)/1-24/(2023): Ben A.P. Nel, Q-factor Bounds for Microstrip Patch Antennas

Ben A.P. Nel
ben.nel@eit.lth.se

Department of Electrical and Information Technology
Electromagnetic Theory
Lund University
P.O. Box 118
SE-221 00 Lund
Sweden

Anja Skrivervik
anja.skrivervik@epfl.ch

Microwave Antenna Group
Ecole Polytechnique Federale de Lausanne (EPFL)
1015 Lausanne
Switzerland

Mats Gustafsson
mats.gustafsson@eit.lth.se

Department of Electrical and Information Technology
Electromagnetic Theory
Lund University
P.O. Box 118
SE-221 00 Lund
Sweden

This is an author produced preprint version of the paper:

B. A. Nel, A. K. Skrivervik, and M. Gustafsson. "Q-factor bounds for microstrip patch antennas". *IEEE Transactions on Antennas and Propagation* (2023)

from http://dx.doi.org/**doi**

This paper has been peer-reviewed but does not include the final publisher proof-corrections or journal pagination.
Homepage `https://www.eit.lth.se` and `https://portal.research.lu.se`.

Editor: Mats Gustafsson

Abstract

Antenna bounds are a useful tool in assessing feasibility or performance of an antenna design. Microstrip patch antennas are often limited by their relatively narrow bandwidth, and therefore Q-factor is an important design parameter, as it is related to the inverse of the fractional bandwidth. This paper presents the first tight lower Q-factor bounds on microstrip patch antennas supported by an infinite dielectric substrate. The derived lower Q-factor bounds are orders of magnitude tighter than the Chu limit and introduce a new scaling rule. These bounds consider all possible geometries on the predefined design region. Moreover, it is shown that well known patch antennas have Q-factors near the bounds and have thus a near optimal bandwidth. The computation of the bounds is done using a method of moments formulation. However, an approximation to these bounds using commonly available simulation tools is provided.

1 Introduction

Microstrip patch antenna technology saw a rapid development in the late 1970s [23, 33] partially driven by their low-cost and ease of fabrication. Modeling of these antennas soon followed, and reliable models showing good agreement with measurements became available by the early 1980s [31]. These models allowed antenna designers to improve performance parameters, such as bandwidth. Microstrip patch antennas are still in wide use today and can be modeled using commercial software *e.g.*, FEKO or CST [1, 2].

Due to the narrowband nature of microstrip antennas, the Q-factor, that is inversely proportional to the fractional bandwidth, is an important design parameter [7]. Bandwidth and Q-factor can be computed for a given design [43] and are then generally optimized by varying parameters using, *e.g.*, heuristic methods [20, 35]. While this is a reliable design approach, it is time-consuming and often obtains local optima rather than a desired global optimum.

Since lower Q-factor bounds of microstrip patch antenna designs are of particular interest, an approach to compute these bounds (also referred to as limit) is presented here. This allows designers to assess the feasibility of reaching a required bandwidth within a specified design region. These bounds also provide benchmarks, in the design process, and when evaluating designs from literature.

A physical bound on Q-factor was derived by Chu [6] in the late 1940s. This bound, applicable to small antennas enclosed by a sphere, radiating into free space, is generally known to be unobtainable for microstrip patch antenna designs due to the latter's form factor. Obtaining tight bounds on several parameters for arbitrarily shaped antennas has successfully been done, using current optimization on antennas made of conductors having no dielectric substrate [5, 10, 13, 24, 25]. Amongst all possible currents, the optimal one produces the lowest possible Q-factor.

In order to determine lower Q-factor bounds, all possible design geometries need to be considered. The performance of these design geometries can be computed

from their underlying current distribution. To compute Q-factor, this current distribution is linked to stored energy and radiated power. Thus, a natural method to compute lower Q-factor bounds is to optimize over all possible current distributions on the antenna design region. Conveniently, these currents are the unknowns in the method of moments (MoM) formulation. A similar formulation would be very difficult in a semi-analytic method *e.g.*, cavity model or numerical methods such as finite element method (FEM) or finite-difference time-domain (FDTD), where the natural unknowns are the fields. Using current optimization with MoM, lower Q-factor bounds are computed by eigenvalue problems.

Microstrip patch antennas can be analyzed numerically, for instance with an integral equation formulation using MoM [31]. If the ground plane and dielectric slab are assumed to be infinite, their effect can be accounted for implicitly in the Green's function, given by Sommerfeld integrals [38]. In this case, the unknowns of the problem are only the currents on the patch, providing a computational advantage over methods, where also the ground plane and dielectric regions need to be discretized [29]. It should be noted that while in reality the ground plane is always finite, comparative studies [8] have found the assumption of an infinite ground plane to be a fair approximation of reasonably large ground planes.

Here, the original definition of a microstrip patch antenna is used, in that a single dielectric layer having all currents horizontally on the patch is assumed. These antennas are typically fed with a vertical feeding pin. While shorting pins, stacked patches or miniaturized ground planes [22, 37, 44] can be used to enhance the bandwidth, they are not considered here. Further, it is also assumed that there is only one dominant resonance over the bandwidth. Patches similar to the ones presented here are in wide use due to their simplicity and low cost.

This paper presents a method to determine an upper limit on achievable bandwidth for microstrip patch antennas. These bounds account for all possible geometries within a predefined design region, thereby obtaining a performance limit to compare miniaturized patch designs with. Obtained bounds are shown to be tight (near) to the performance of some practical antenna designs. As the computation of the bounds requires a MoM formulation, it is also shown that an approximation of the bounds can be obtained requiring only the simulation of a half-wavelength patch antenna. The bounds are formulated in Q-factor which is an accurate estimate of achievable bandwidth given a single dominant resonance over the bandwidth [43]. These bounds build on [41] by allowing for the addition of a dielectric substrate. This non-trivial addition makes the bounds more relevant for microstrip antenna designers, where a dielectric is usually required.

Section 2 presents the microstrip patch antenna formulation that is used to compute bounds. Section 3 validates expressions derived to compute Q-factor. Section 4 shows how to compute lower Q-factor bounds and section 5 provides a method to predict bounds based on simulating half-wavelength resonant patch antennas. Then, in section 6, practical examples of the proposed bounds and comparisons with patch antennas are shown. Section 7 concludes the paper. Finally, the Appendices provide additional information on Sommerfeld integrals and low-frequency Q-factor scaling.

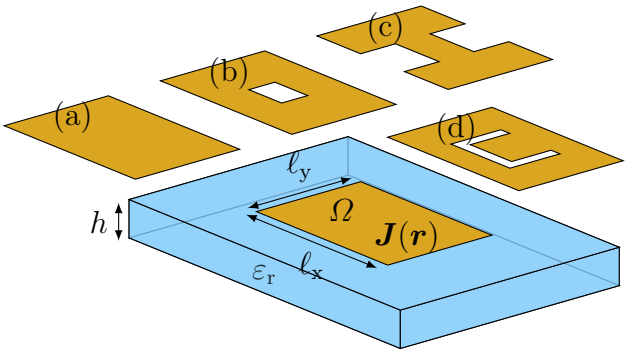

Figure 1: Microstrip patch antennas confined to a design region, Ω, with side lengths ℓ_x and ℓ_y on top of an infinite dielectric substrate having relative permittivity ε_r and thickness h. The dielectric substrate is on top of an infinite PEC ground plane. Some possible patch geometries fitting within the design region are rectangular patch (a), slot loaded patch (b), H-shaped patch (c), and U-slot patch (d).

2 Microstrip patch antenna model

In this paper, microstrip patch antennas are modeled by assuming an infinite PEC ground plane and an infinite lossless dielectric substrate. On top of the substrate is a PEC patch confined to a design region Ω, *e.g.*, a rectangle with side lengths ℓ_x and ℓ_y, see Fig. 1. The presence of the dielectric layer affects the microstrip patch antenna performance in several ways leading to a non-trivial relationship between dielectric permittivity and Q-factor. The combination of these effects with the widespread applications emphasizes the importance of adding a dielectric to the Q-factor formulations developed in the past [27, 41] that use image theory to account for an infinite ground plane but do not consider the dielectric substrate.

Some classical patch antenna geometries constructed within a rectangular design region Ω are shown in Fig. 1. The rectangular patch (a) is resonant around half-a-wavelength [23] in the dielectric. A lower resonance frequency is obtained by slot loading (b) effectively lengthening the current path and miniaturizing the patch [32]. For further miniaturization the H-shaped patch (c) can be used [32]. Dual resonances can be obtained with the U-slot patch (d) [21]. These patches can be constructed by removing metal from the rectangular design region and then the radiated field is determined by the current density $\boldsymbol{J}(\boldsymbol{r})$ on the remaining metal part. This enables modeling of antenna parameters such as Q-factor and gain from all patch geometries within the design region Ω by identifying non-metal regions with current density $\boldsymbol{J}(\boldsymbol{r}) = \boldsymbol{0}$.

In this paper, lower bounds on the Q-factor for microstrip patch antennas are determined by optimizing over current densities $\boldsymbol{J}(\boldsymbol{r})$ in Ω for given height (h), relative permittivity (ε_r), and frequency (f), see Fig. 1. These bounds implicitly account for all possible patch geometries within the design region (Ω), such as (a)-(d) in Fig. 1. Since the bounds are tailored to microstrip patch antennas, they can be tight to designs.

Here, it is important to emphasize the key difference between a method to com-

pute the performance of a given structure, as opposed to the bounds for a given design region. For a given structure and excitation, analyzing microstrip patch antennas is well understood [31]. For instance using a commercial solver. In contrast, bounds for a given design region rather computes a performance limit for all antennas fitting within the design region using *e.g.*, MoM as a tool in current optimization. The latter is not understood as well, but may provide simple, yet valuable, results to antenna designers.

MoM [17, 31] is used to compute microstrip patch antenna bounds, where the surface current density on the design region Ω is expanded in a set of basis functions $\boldsymbol{\psi}_m(\boldsymbol{r})$ as

$$\boldsymbol{J}(\boldsymbol{r}) = \sum_{m=1}^{M} I_m \boldsymbol{\psi}_m(\boldsymbol{r}). \tag{2.1}$$

The expansion coefficients I_m are collected in $\mathbf{I} \in \mathbb{C}^{M\times 1}$ and related to the excitation voltages $\mathbf{V} \in \mathbb{C}^{M\times 1}$ as

$$\mathbf{ZI} = \mathbf{V}. \tag{2.2}$$

The MoM impedance matrix, $\mathbf{Z} \in \mathbb{C}^{M\times M}$, is decomposed in its real and imaginary parts

$$\mathbf{Z} = \mathbf{R} + \mathrm{j}\mathbf{X} \tag{2.3}$$

defining the resistance $\mathbf{R} \in \mathbb{R}^{M\times M}$ and reactance $\mathbf{X} \in \mathbb{R}^{M\times M}$ matrices. This MoM impedance matrix describes the interaction between all basis functions on the patch. The interaction between the patch basis functions and the external environment (*e.g.*, dielectric and ground plane) is implicitly accounted for through the Green's functions derived using *e.g.*, Sommerfeld integrals [31].

3 Calculating and validating Q-factor

The Q-factor of a single resonant antenna is inversely proportional to its fractional bandwidth [43]. However, unlike bandwidth, Q-factor can be computed at a single frequency. This is exploited here to approximate bandwidth, which is an important microstrip patch antenna design parameter. It should be noted that this formulation can be extended to multiband antennas, as long as there is one dominant resonance within each band.

The Q-factor of an antenna is related to its fractional bandwidth by [43]

$$B_{\Gamma_0} \approx \frac{2}{Q} \frac{\Gamma_0}{\sqrt{1-\Gamma_0^2}}, \tag{3.1}$$

where Γ_0 is the threshold for the reflection coefficient. An approximate Q-factor can be determined from inverting (3.1) as

$$Q_{\Gamma_0} = \frac{2}{B_{\Gamma_0}} \frac{\Gamma_0}{\sqrt{1-\Gamma_0^2}}. \tag{3.2}$$

In this paper, the threshold is set to $\Gamma_0 = -10\,\mathrm{dB}$ to calculate approximate Q-factor values from simulated bandwidths.

The Q-factor (3.1) is linked to the quotient of stored energy and dissipated power (P_d) as

$$Q = \frac{2\omega \max\{W_\mathrm{e}, W_\mathrm{m}\}}{P_\mathrm{d}}, \tag{3.3}$$

where angular frequency is denoted by $\omega = 2\pi f$, electric stored energy by W_e, and magnetic stored energy by W_m.

Surface waves [22] result in some dissipated power in (3.3) not being radiated into free space even for an infinite lossless dielectric, PEC patch, and infinite PEC ground plane. When the substrate is thin, the surface wave that propagates in the dielectric layer only contains the first transverse magnetic surface-wave mode. This mode has no cutoff frequency and the first transverse electric surface-wave mode is launched when the free-space wavelength is, $\lambda < 4h\sqrt{\varepsilon_\mathrm{r} - 1}$, [31].

The dissipated power can then be divided into power radiated into free space (P_r) and power lost in the surface wave (P_sw) as $P_\mathrm{d} = P_\mathrm{r} + P_\mathrm{sw}$. Then radiation efficiency due to losses in the surface wave is expressed as

$$\eta = \frac{P_\mathrm{r}}{P_\mathrm{r} + P_\mathrm{sw}}. \tag{3.4}$$

Power lost in surface waves is undesirable even for a finite ground plane where they lead to diffraction on the edges [31]. Therefore rather than using the Q-factor in (3.3), a radiated Q-factor is determined as

$$Q_\mathrm{rad} = \frac{Q}{\eta} = \frac{2\omega \max\{W_\mathrm{e}, W_\mathrm{m}\}}{P_\mathrm{r}}. \tag{3.5}$$

Before the Q-factors (3.3) and (3.5) can be computed, expressions for dissipated power and stored energy are required. These quantities are determined from the current density $\boldsymbol{J}(\boldsymbol{r})$ in the design region Ω contained in the column matrix $\mathbf{I}$, *e.g.*, computed for a given geometry and excitation using (2.1). The dissipated power in (3.3) is evaluated from the MoM resistance matrix $\mathbf{R}$ in (2.3) as [17]

$$P_\mathrm{d} = \frac{1}{2}\mathbf{I}^\mathrm{H}\mathbf{R}\mathbf{I}, \tag{3.6}$$

where the Hermitian transpose is denoted by superscript $^\mathrm{H}$. The radiated power (3.4) is similarly determined from the radiation resistance matrix $\mathbf{R}_\mathrm{r} \in \mathbb{R}^{M\times M}$ as

$$P_\mathrm{r} = \frac{1}{2}\mathbf{I}^\mathrm{H}\mathbf{R}_\mathrm{r}\mathbf{I}. \tag{3.7}$$

For a lossless dielectric, the radiation resistance matrix can be computed from the far field (Appendix A) or by splitting up the Sommerfeld integral as shown in [31].

Stored electromagnetic energies of microstrip patch antennas are interpreted here as the energy that does not radiate away through the dielectric (surface wave) or into

free space (space wave). These energies are stored around the patch, for instance in the dielectric region near the patch (standing wave).

Stored energy of small antennas in free space have been accurately modeled [36, 42] and been generalized to patch antennas above an infinite ground plane [41] and heterogeneous temporally dispersive media [14]. The total stored energy can be computed by differentiation of the reactance MoM matrix $\mathbf{X}$ in (2.3) as proposed in [18] which together with the reactance define stored electric and magnetic energies [17, 36]

$$W_{\mathrm{e}} = \frac{1}{8}\mathbf{I}^{\mathrm{H}}\left(\frac{\partial \mathbf{X}}{\partial \omega} - \frac{\mathbf{X}}{\omega}\right)\mathbf{I} \quad \text{and } W_{\mathrm{m}} = \frac{1}{8}\mathbf{I}^{\mathrm{H}}\left(\frac{\partial \mathbf{X}}{\partial \omega} + \frac{\mathbf{X}}{\omega}\right)\mathbf{I}. \tag{3.8}$$

Here, stored energy expressions for small antennas in free space are extended to microstrip patch antennas, allowing for stored energy to be localized in the dielectric substrate near the patch design region Ω. This procedure is based on (3.8) where closed form expressions for the angular frequency derivative, $\frac{\partial \mathbf{X}}{\partial \omega}$, are presented in Appendix A based on Sommerfeld integrals. From (3.8) it can be shown that both the electric and magnetic stored energy have a term associated with the vector and scalar potential Green's functions [31] and the angular frequency derivative thereof.

To validate the expressions for stored energies (3.8) for microstrip patch antennas, the Q-factor (3.3) is compared with Q-factors based on fractional bandwidth (3.2) and differentiation of the input impedance [36]. In this latter method the Q-factor for a single resonant antenna tuned with a series capacitor or inductor is given by [43]

$$Q_{\mathrm{Z}'_{\mathrm{in}}} = \frac{\sqrt{(\omega R'_{\mathrm{in}})^2 + (\omega X'_{\mathrm{in}} + |X_{\mathrm{in}}|)^2}}{2R_{\mathrm{in}}}, \tag{3.9}$$

where $'$ denotes angular frequency derivative and R_{in} and X_{in} are the real and imaginary parts of the input impedance, respectively.

A comparison between Q-factors (3.3) based on stored energies (3.8) (solid red curve) and differentiation of the input impedance (3.9) (dashed green curve) for H-shaped and rectangular patches are shown in Fig. 2. The H-shaped and rectangular patches are fed with a delta gap excitation and microstrip line, respectively, with position indicated by the black rectangle. For further validation with (3.9), commercial software (FEKO) was used with a thin-wire feed over a small cut in the H-shaped patch instead of a delta gap feed (blue curve). Similarly, to validate the results for the rectangular patch the microstrip port excitation model in FEKO was used. For both patches the self resonances ($X_{\mathrm{in}} = 0$) were matched to R_{in}, in order to compute the fractional bandwidth. Then the fractional bandwidth was used to calculate Q-factor (Q_{Γ_0}) from (3.2). These Q-factors are shown by black markers in Fig. 2 and confirm the calculated Q-factor. This example indicates that Q-factor determined from the quadratic forms (3.8) is an accurate indicator of Q-factor and fractional bandwidth for microstrip patch antennas. Finally, it should be noted that when interpreting computed Q-factor (3.3) and (3.9) in terms of bandwidth (3.2) for non-resonant structures ($X_{\mathrm{in}} \neq 0$) a series tuning capacitor or inductor is assumed.

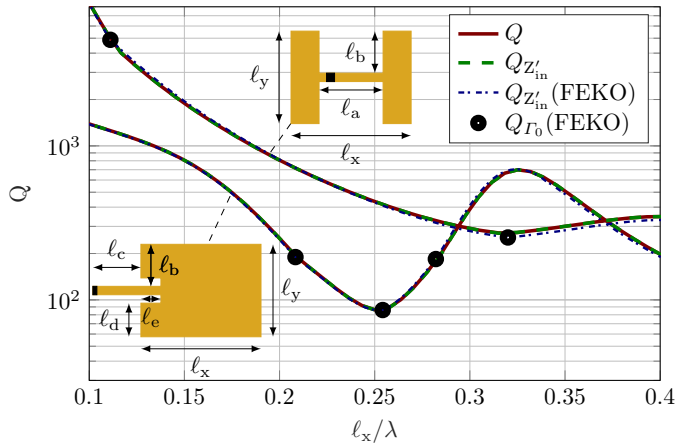

Figure 2: Validation of Q-factors computed using the stored energy in (3.8) (Q), differentiation of the input impedance (3.9) ($Q_{Z'_{\text{in}}}$) and fractional bandwidth (3.2) (Q_{Γ_0}) for H-shaped and rectangular microstrip patch antennas on a dielectric slab with relative permittivity, $\varepsilon_{\text{r}} = 4$, dimensions $h = 0.05\ell_{\text{x}}$, $\ell_{\text{y}} = 0.77\ell_{\text{x}}$, $\ell_{\text{a}} = 7\ell_{\text{x}}/15$, $\ell_{\text{b}} = 5\ell_{\text{y}}/11$, $\ell_{\text{c}} = 2\ell_{\text{x}}/7$, $\ell_{\text{d}} = 7\ell_{\text{y}}/22$, and $\ell_{\text{e}} = 5\ell_{\text{x}}/42$. The Q-factors at self resonances are indicated with markers and are computed from the bandwidth (Q_{Γ_0}).

4 Lower Q-factor bounds

From the expressions of Q-factor (3.3), dissipated power (3.6), and stored energy (3.8), an optimization problem to compute lower bounds on Q-factor can be written as

$$\begin{aligned} &\text{minimize} && \max\left\{W_{\text{e}}\left(\mathbf{I}\right), W_{\text{m}}\left(\mathbf{I}\right)\right\} \\ &\text{strubject to} && P_{\text{d}}\left(\mathbf{I}\right) = P_{\text{in}}. \end{aligned} \tag{4.1}$$

Both the objective (related to numerator of (3.3)) and the constraint are quadratic functions of the current ($\mathbf{I}$), which is the optimization variable. Therefore, this is a quadratically constrained quadratic program (QCQP) which can be solved using its dual as a parametrized eigenvalue problem [12]. Note that the input power (P_{in}) in (4.1) can be set to any arbitrary positive value. This does not change the bounds, but rather just scales the optimal currents. For the eigenvalue problem, a convex combination of W_{e} and W_{m} can be taken [5]. Then the eigenvalue problem to compute lower Q-factor bounds can be written as [13]

$$Q_{\text{lb}} = \frac{1}{2}\max_{\nu} \min \operatorname{eig}\left(\nu\mathbf{X} + \mathbf{X}_{\omega}, \mathbf{R}\right), \tag{4.2}$$

with Lagrange parameter $\nu \in [-1, 1]$ and $\mathbf{X}_{\omega} = \omega\frac{\partial \mathbf{X}}{\partial \omega}$. It should be noted that low-rank matrices $\mathbf{R}$ can be exploited [9, 15] to reduce the computational cost of (4.2).

Once the optimization problem has been solved, it is possible to obtain currents that satisfy the bound from the eigenvectors. This implies equality in (4.2) and therefore no dual gap [3]. In some cases it may be necessary to test for degenerate eigenvalues to recover the currents as shown in [5]. This phenomenon is attributed to geometrical symmetries in the problem.

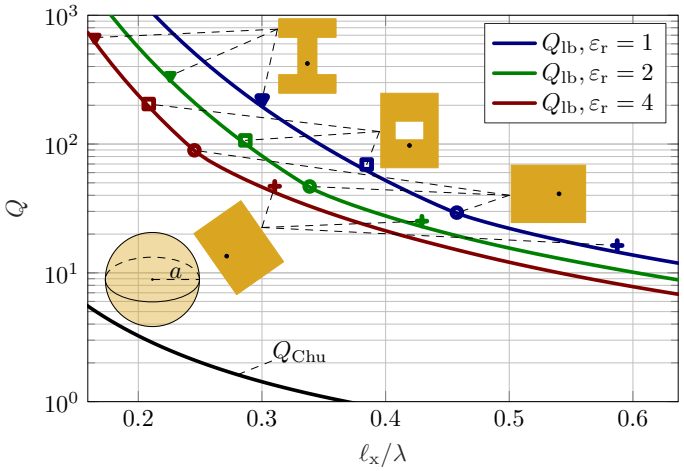

Figure 3: Demonstration of the tightness of lower Q-factor bounds for a rectangular design region Ω with aspect ratio $\ell_y = 0.77\ell_x$, substrate thickness $h = 0.05\ell_x$ and relative permittivity $\varepsilon_r \in \{1, 2, 4\}$ computed using (4.2). FEKO simulation results for self-resonant antenna types (a-c in Fig. 1) with Q-factors from (3.9) are indicated with markers. The H-shaped patch (c) has additional dimensions, $\ell_a = 0.5\ell_x$ and $\ell_b = \ell_y/3$, see Fig. 2. To place the new bounds into perspective, the Chu limit (Q_{Chu}) [6] is included.

The Q-factor bounds from (4.2) can be determined once the MoM impedance matrix (2.3) and its angular frequency derivative in Appendix A have been computed. Q-factor bounds,

$$Q_{lb} = Q_{lb}(f, \Omega, h, \varepsilon_r), \tag{4.3}$$

obtained in this way are functions of several microstrip patch antenna parameters. Investigations of the bounds for any of these parameters can lead to useful antenna design insight. Illustrations in this paper focus on two cases; firstly how the bounds depend on the frequency f for a fixed design region and dielectric slab, and secondly how the bounds depend on the design region Ω for a fixed dielectric slab and frequency.

To demonstrate the bounds for the case with a fixed geometry, a design region Ω with $\ell_y = 0.77\ell_x$ and dielectric thickness $h = 0.05\ell_x$, see Fig. 1, is considered together with a sweep of frequency or equivalently free-space wavelength (λ). For substrate relative permittivities $\varepsilon_r \in \{1, 2, 4\}$, lower Q-factor bound, Q_{lb}, are shown for electrical sizes ℓ_x/λ by solid lines in Fig. 3. It should be further emphasized that although the bounds are computed for a rectangular patch region, they imply thatany patch geometry fitting within the design region, Ω has Q-factor at or above the bound.

The Chu bound [6, 39], $Q \geq Q_{Chu} = 1/(ka)^3 + 1/(ka)$, for any antenna enclosed in a sphere of radius a circumscribing the patch and its mirror image, is also shown in Fig. 3. The Chu limit is clearly not tight for microstrip patch antennas and orders of magnitude off the bounds presented here. This is due to the use of a circumscribing sphere, where the radius of the volumetric design region is $a \approx 0.632\ell_x$ instead of

the actual planar design region.

The bounds are compared with Q-factors from (3.9) of antenna designs (a-c) in Fig. 1 with input impedance simulated in FEKO. These patches with probe feed, having placement indicated by markers on their geometry, are shown in Fig. 3. The two half-wavelength resonant patches (a in Fig. 1) are matched to $50\,\Omega$. The Q-factors calculated using (3.9) are shown to be approximately on the bounds for all three relative permittivities. Two other matched antenna designs (slot loaded (b) and H-shaped (c)) are shown to also be approximately on the bounds. These examples demonstrate that the computed bounds are tight, in the sense that it is possible to design antennas with Q-factors close to the bound. The examples also show that the resonance frequencies scale approximately with the wavelength in the dielectric $\lambda_\varepsilon = \lambda/\sqrt{\varepsilon_\mathrm{r}}$, as expected.

The optimal currents obtained from (4.2) given a rectangular design region are generally associated with a polarization along the longer dimension of the patch for radiation in the normal direction, therefore in Fig. 3, $\hat{\boldsymbol{x}}$-polarized as $\ell_\mathrm{x} > \ell_\mathrm{y}$. To enforce polarization along the shorter dimension of the patch, the optimization problem (4.1) is reformulated by adding an affine constraint to ensure no undesired polarization as

$$\begin{aligned} &\text{minimize} && \max\left\{W_\mathrm{e}\left(\mathbf{I}\right), W_\mathrm{m}\left(\mathbf{I}\right)\right\} \\ &\text{strubject to} && P_\mathrm{d}\left(\mathbf{I}\right) = P_\mathrm{in} \\ &&& \mathbf{F}_\mathrm{o}\mathbf{I} = 0, \end{aligned} \tag{4.4}$$

where $\mathbf{F}_\mathrm{o}$ is the far-field vector (defined in Appendix A) for the undesired polarization. When an $\hat{\boldsymbol{x}}$-polarization bound is desired but $\ell_\mathrm{y} > \ell_\mathrm{x}$, then $\mathbf{F}_\mathrm{o}$, defined here for radiation normal to the patch into free space, should be for $\hat{\boldsymbol{y}}$-polarization in (4.4). Optimization problem (4.4) can be reduced to the form (4.1) by eliminating the linear equality constraint [4], similar to (4.2), solved as an eigenvalue problem. It should be noted that by maximizing partial gain over Q-factor, dependence on polarization can also be investigated [41].

The optimization problems in (4.1) and (4.4) can be reformulated to minimize the radiated Q-factor (Q_rad) in (3.5) by replacing P_d with P_r. This can potentially yield different optimal currents.

5 Bounds from self-resonant patches

The formulation to obtain lower Q-factor bounds presented in section 4 requires a MoM implementation as *e.g.*, presented in section 2. However, a simpler approximate formulation to obtain lower Q-factor bounds may be desired. Therefore, this section introduces a simple approximate method for obtaining lower Q-factor bounds over a range of frequencies (4.3), requiring only simulations of half-wavelength resonant patch antennas.

Patch antenna resonances are associated with their dielectric wavelengths, as shown in Fig. 3. Therefore, it is worth comparing bounds at the same dielectric wavelength λ_ε as shown in Fig. 4. When comparing Fig. 3 and Fig. 4, it is observed that the order of the curves are swapped. This is simply due to the bounds being

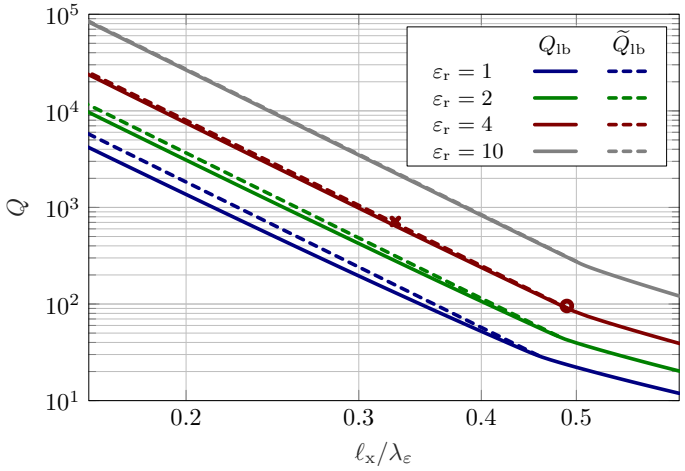

Figure 4: Lower Q-factor bounds for rectangular design regions Ω with dimensions $\ell_y = 0.77\ell_x$ and dielectric thickness $h = 0.05\ell_x$ plotted versus $\ell_x/\lambda_\varepsilon$. Dashed lines show how (5.1) approximates the lower Q-factor bounds from simulations of half-wavelength resonant patches. The markers show the Q-factor obtained from simulating a half-wavelength resonant patch antenna as well as the predicted Q-factor from (5.1) interpreted as for the same geometry at a desired design frequency.

represented with respect to dielectric wavelength in Fig. 4 as opposed to the free-space wavelength in Fig. 3. Other than the addition of the bounds with relative permittivity $\varepsilon_r = 10$ the data is the same.A reason for using the dielectric wavelength is that resonances of half-wavelength patches are approximately at $\ell_x/\lambda_\varepsilon \approx 0.5$.

The log-log plot in Fig. 4 has straight lines, and the bounds scaling can be read of as approximately $(\lambda_\varepsilon/\ell_x)^5$ (doubling size reduces Q bounds by a factor 32) up to the half-wavelength resonances. This scaling is also derived in Appendix B through a low-frequency expansion assuming no total charge on the patch, given $\varepsilon_r = 1$, and can be partially attributed to the ground plane acting as a short for small h/λ. It should be noted that at low-frequencies given a total charge on the patch, radiation from the charge difference between patch and ground plane can result in $(\lambda_\varepsilon/\ell_x)^3$ Q-factor scaling, however this form of monopole radiation is not desired for patch antennas.

To use the $(\lambda_\varepsilon/\ell_x)^5$ scaling to approximate bounds, a valid reference Q-factor is required. For this, simulated half-wavelength resonant patch antennas' Q-factors, Q_{hw}, computed using (3.2) or (3.9), are chosen. These are reasonable reference Q-factors, as these antennas perform close to the bounds, as shown in Fig. 3. The simple scaling rule that follows from these simulations of half-wavelength resonant patch antennas with frequency f_{hw} and dielectric wavelength $\lambda_{\varepsilon,\text{hw}}$, is given by

$$\widetilde{Q}_{\text{lb}}(f) = \frac{Q_{\text{hw}} f_{\text{hw}}^5}{f^5} = \frac{Q_{\text{hw}} \lambda_\varepsilon^5}{\lambda_{\varepsilon,\text{hw}}^5}. \tag{5.1}$$

This scaling rule is presented in Fig. 4 (dashed lines) for bounds varying in frequency for a fixed design region and dielectric slab, *i.e.*, for a fixed ε, h, ℓ_x and ℓ_y. The results

show that by only simulating one half-wavelength patch, a good approximation of Q-factor bounds over a range of frequencies with chosen geometric constraints and permittivity are obtained. This scaling is observed to be more accurate for higher relative permittivity. It should be noted that this scaling can also be added as an extension of the cavity model predicted half-wavelength Q-factors [23], this does not require a full-wave solver but is less accurate.

For design purposes, it is convenient to know approximate bounds on Q-factor to obtain a benchmark before beginning the design process. To this aim, consider a design region Ω with fixed dielectric slab and working frequency of the antenna f. For the design region the maximum length is ℓ_{x} and the maximum width is ℓ_{y}. The relative permittivity and height of the dielectric slab are ε_{r} and h, respectively. An approximation of lower Q-factor bounds for the antenna under design consideration can be obtained using the scaling (5.1) through the following procedure:

1. Determine the half-wavelength resonance frequency, f_{hw}, for the considered dielectric slab and design region
2. Obtain the Q-factor Q_{hw} of the half-wavelength patch using either (3.2) or (3.9)
3. Obtain $\widetilde{Q}_{\mathrm{lb}}(f)$ from Q_{hw} using (5.1)

An example of using the scaling rule (5.1) is to compute an approximation of lower Q-factor bounds at 2.45 GHz for relative permittivity $\varepsilon_{\mathrm{r}} = 4$, dimensions $\ell_{\mathrm{x}} = 20\,\mathrm{mm}$, $\ell_{\mathrm{y}} = 15.4\,\mathrm{mm}$ and $h = 1\,\mathrm{mm}$. Then step 1) the half-wavelength resonance frequency is determined as approximately 3.665 GHz. For the second step 2) the Q-factor is computed as 95.5 at the half-wavelength resonance. Then finally 3) using the scaling $\widetilde{Q}_{\mathrm{lb}}(f) \approx 95.5(3.665/2.45)^5 \approx 715$. This corresponds to a $-10\,\mathrm{dB}$ bandwidth of approximately 2.3 MHz. The results from these steps are shown by markers in Fig. 4.

The scaling of (5.1) is further demonstrated on results presented in Fig. 4, by factoring out the $\lambda_\varepsilon^5/\ell_{\mathrm{x}}^5$ scaling, as shown in Fig. 5. Additional dielectric thicknesses are also considered and shown to have similar scaling along with the expected result that increased dielectric thickness results in a lower Q-factor [23]. Lastly, it should be noted that the small difference between the predicted scaling and bounds in Fig. 4 depends on h and λ. By reducing h or increasing λ the proposed scaling (5.1) becomes a more accurate approximation. This means that scaling comes closer to the low-frequency expansion of Appendix B, and also that the scaling contribution of the surface wave is reduced.

6 Practical examples

In this section, practical applications of the lower Q-factor bounds compared with simulated antenna designs are presented. Subsection 6.1 illustrates how the Q-factor depends on the patch width for antennas linearly polarized along their length. Subsection 6.2 examines how the size of the design region impacts Q-factor bounds

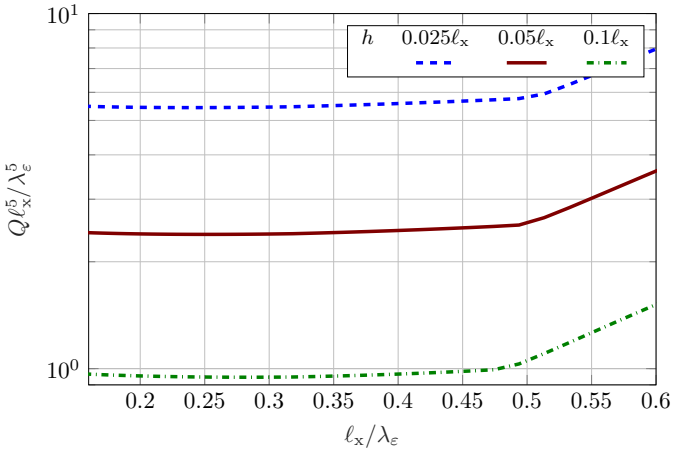

Figure 5: Lower Q-factor bounds for rectangular patch region with dimensions $\ell_y = 0.77\ell_x$, relative permittivity $\varepsilon_r = 4$ and varying height. The axis is scaled to show the $(\ell_x/\lambda_\varepsilon)^5$ scaling.

for a given frequency and substrate. Subsection 6.3 shows how the bounds can be applied to dual resonant patch antennas. Finally, subsection 6.4 shows the effect when bounds are determined on radiated Q-factor (3.5) instead of on Q-factor (3.3).

6.1 Design region width

Improvement in bandwidth can be achieved by altering the width of half-wavelength patch antennas [23]. This subsection investigates this improvement for arbitrary shaped antennas, designed within a rectangular design region Ω (see Fig. 1). In Fig. 6, the patch width (ℓ_y) effect on the bounds for polarization along the length (ℓ_x) enforced by (4.4) is shown. However, the slopes of the bounds in Fig. 6 are relatively unaffected by the change in width. This implies that the scaling rule of (5.1) can be generalized to other length-to-width ratios than shown in Fig. 4. The bounds are observed to scale roughly as ℓ_x/ℓ_y (doubling ℓ_y reduces Q bounds by a factor 2) as shown in Fig. 7 at selected $\ell_x/\lambda_\varepsilon$. Further, when the width is greater than the length, the lower Q-factor bounds can be significantly greater than when polarization is disregarded solving (4.1), especially at lower frequencies. This is due to the dielectric wavelength of the patch being linked to the polarization direction (ℓ_x) and therefore being the most significant patch dimension regarding Q-factor scaling, especially before the half-wavelength resonance (as shown in subsection 6.3). Finally, the bounds of Fig. 1 are shown to have both the H-shaped and half-wavelength patch antennas near the Q-factor bounds for all presented patch dimensions.

6.2 Patch design for a given substrate and frequency

A classical problem is to design patch antennas for a given frequency and dielectric substrate. In this subsection, a design scenario is used to investigate how the design

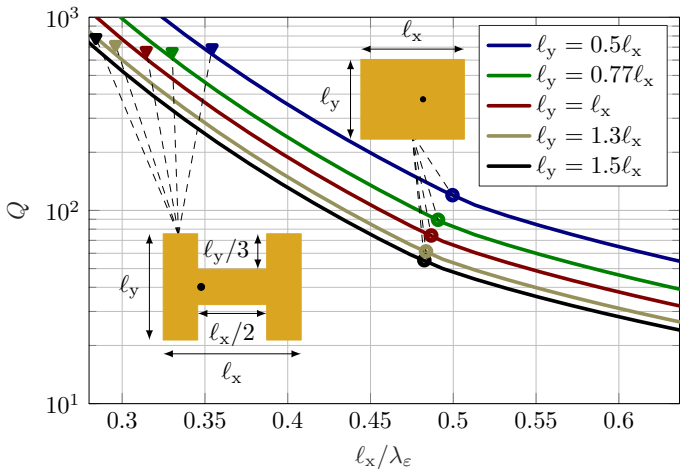

Figure 6: Effect of width ℓ_y on the lower Q-factor bounds, $Q_{\text{lb,x}}$, for polarization along ℓ_x enforced through (4.4), relative permittivity $\varepsilon_r = 4$ and thickness $h = 0.05\ell_x$. The bounds are compared to the performances of H-shaped and half-wavelength resonant patch antennas using (3.2).

region (Ω) affects the Q-factor bounds for a given dielectric substrate and frequency. The chosen substrate has thickness, $h = 1.57\,\text{mm}$, and relative permittivity, $\varepsilon_r = 2.33$, as for RTDuroid 5870 by Rogers Corporation, but it is considered lossless. Then, for a frequency of $f = 2.45\,\text{GHz}$, the length and width of the patch design region are varied. The lower Q-factor bounds, constrained to $\hat{\boldsymbol{x}}$-polarization in the normal direction by solving optimization problem (4.4), are shown in Fig. 8. This contour plot for a range of design region dimensions provides lower Q-factor bounds. Given a design region, the bounds indicate whether it is possible to obtain a required Q-factor. For a desired Q-factor, the bounds also provide a range of possible design regions that can aid patch miniaturization.

The regular spacing of the contours in log scale show that for this scenario a relatively simple bounds scaling can be derived. The contour lines are all spaced by $10^{0.2}$, therefore, the first line less than $Q_{\text{lb,x}} = 1000$ is $Q_{\text{lb,x}} \approx 631$. Going between these two lines, it can clearly be read off that a change in ℓ_x (polarization dimension) results in greater bounds scaling compared with an equal change in ℓ_y (width dimension), as shown in subsection 6.1. Thus, doubling ℓ_x results in moving across 4 contour lines while doubling ℓ_y results in only moving across 2 contour lines.

To further demonstrate the relevance of the bounds, FEKO is used to simulate patch antennas. This is first done for three half-wavelength patches by using a probe feed and then obtaining Q-factors from (3.9). These results are shown to be near the bounds and are indicated by their geometry in the contour plot. Further, slot loaded patches (b) and an H-shaped patch (c), are simulated. All patches shown in Fig. 8 are within a margin of 10% from the lower Q-factor bounds, see Table 6.2.

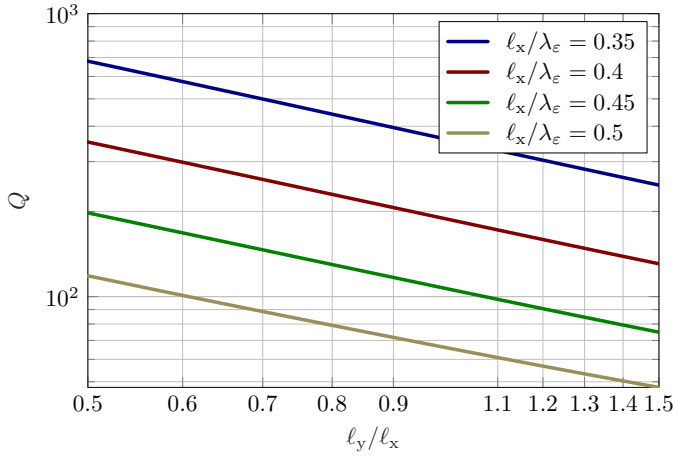

Figure 7: Effect of width (ℓ_y) on the lower Q-factor bounds, $Q_{\text{lb,x}}$, for different electrical lengths $\ell_x/\lambda_\varepsilon$ with polarization along ℓ_x enforced through (4.4), relative permittivity $\varepsilon_r = 4$ and thickness $h = 0.05\ell_x$.

Patch type	ℓ_x/ mm	ℓ_y/ mm	$Q_{\text{lb,x}}$	$Q_{Z'_{\text{in}}}$
Half-wavelength	38.5	50	45	45
Half-wavelength	38.9	30	66	67
Half-wavelength	39.4	20	90	91
Slot loaded	35.2	28	90	94
Slot loaded	36.7	18	118	121
H-shaped	25.9	20	274	297

Table 1: Numerical Q-factors of Patches Shown in Fig. 8

6.3 Dual resonance

Some patch antennas are designed for dual resonance [22]. In the first example, Q-factors for dual resonant antennas are compared with the lower Q-factor bounds allowing for different polarization for the two resonances. In the second example, a design with the same polarization for both resonances is considered.

For the first example, Fig. 9 shows a comparison between $\hat{\boldsymbol{x}}$ and $\hat{\boldsymbol{y}}$-polarized lower Q-factor bounds (4.4) for a patch with dimensions $\ell_y = 0.77\ell_x$, $h = 0.05\ell_x$ and relative permittivity $\varepsilon_r = 4$. Firstly, it shows that at lower frequencies, a significant reduction in Q-factor can be achieved by having polarization along the longer dimension of the design region. Further, it indicates that at higher frequencies (around the half-wavelength resonance of the shorter (y) dimension) there is little difference between the bounds. This result also shows that for dual resonant patch antennas, two orthogonal modes tight to the bounds can be obtained. This patch is shown with feed placement indicated with a black dot. Further, a reduction in Q-factor is not possible by using circular polarization [16, 34] with these design parameters since $\hat{\boldsymbol{x}}$-polarization is essentially on the bounds, calculated using (4.1), which allows for arbitrary polarization.

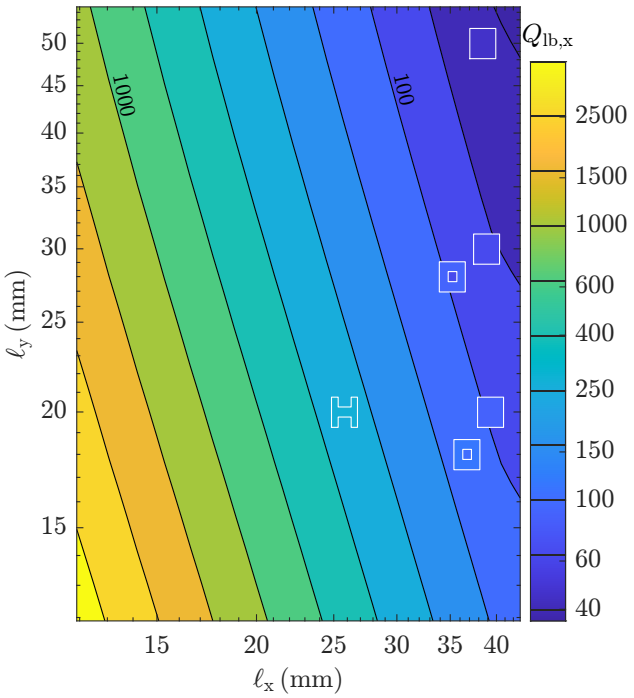

Figure 8: Lower Q-factor bounds, $Q_{\mathrm{lb,x}}$, for relative permittivity $\varepsilon_{\mathrm{r}} = 2.33$, frequency $f = 2.45\,\mathrm{GHz}$, dielectric thickness $h = 1.57\,\mathrm{mm}$ and a rectangular design region Ω with side lengths ℓ_{x} and ℓ_{y} for $\hat{\boldsymbol{x}}$-polarized antennas in the normal direction. The shown antenna geometries have interior colors corresponding to their Q-factors computed using (3.9), see Table 6.2.

For the second example, a dual resonant antenna with the same polarization for both bands can be obtained from the U-slot patch (d) in Fig. 1. In this case, efficiently utilizing the patch design region for both resonances is challenging. This is because a larger portion of the design region is effectively used for the first resonance than for the second resonance. The results in Fig. 10 show this for a chosen U-slot patch (with dimensions $h = 4.5\,\mathrm{mm}$, $\ell_{\mathrm{x}} = 21.5\,\mathrm{mm}$ and $\ell_{\mathrm{y}} = 26.5\,\mathrm{mm}$). From simulations Q-factor is computed using (3.2), the resonances are located at approximately 3.64 GHz ($\ell_{\mathrm{x}}/\lambda_\epsilon \approx 0.39$) and 5.23 GHz ($\ell_{\mathrm{x}}/\lambda_\epsilon \approx 0.56$). The first resonance is near the bounds, while the second is significantly off. This may be seen as a fair trade-off, as it results in a similar fractional bandwidth of approximately 0.05 for both resonances. This fractional bandwidth is similar to what is reported in [19] from CST simulations with a finite ground plane that is double the size of the design region.

6.4 Surface-wave losses

To investigate the contribution of surface-wave losses on Q-factor bounds (4.1), the latter are computed with (Q_{lb}) and without surface-wave losses ($Q_{\mathrm{lb}}^{\mathrm{rad}}$). For both Q_{lb} and $Q_{\mathrm{lb}}^{\mathrm{rad}}$ the optimal currents are then used to compute the radiation efficiency for relative permittivities $\varepsilon_{\mathrm{r}} \in \{2, 4\}$ as shown in Fig. 11. Observe that in

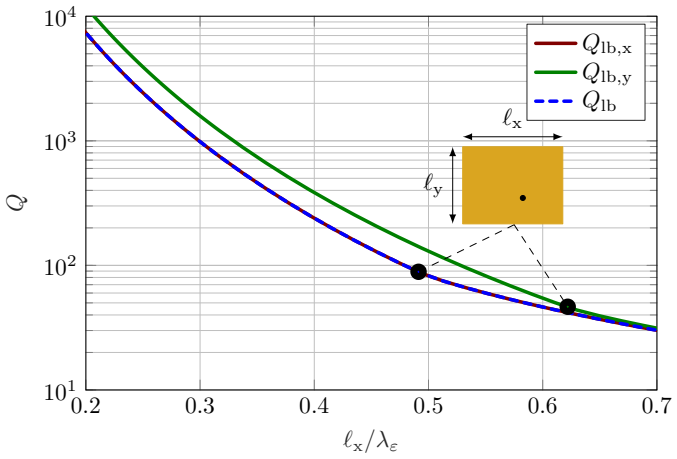

Figure 9: Dual polarized antenna design with $\hat{\boldsymbol{x}}$ and $\hat{\boldsymbol{y}}$-polarization, compared with lower Q-factor bounds for a design region with dimensions $\ell_{\mathrm{y}} = 0.77\ell_{\mathrm{x}}$, $h = 0.05\ell_{\mathrm{x}}$ and relative permittivity $\varepsilon_{\mathrm{r}} = 4$ obtained from (4.1) and (4.4). The duel resonant antenna geometry is shown with feed location and two simulated resonance Q-factors obtained using (3.9) are indicated by markers.

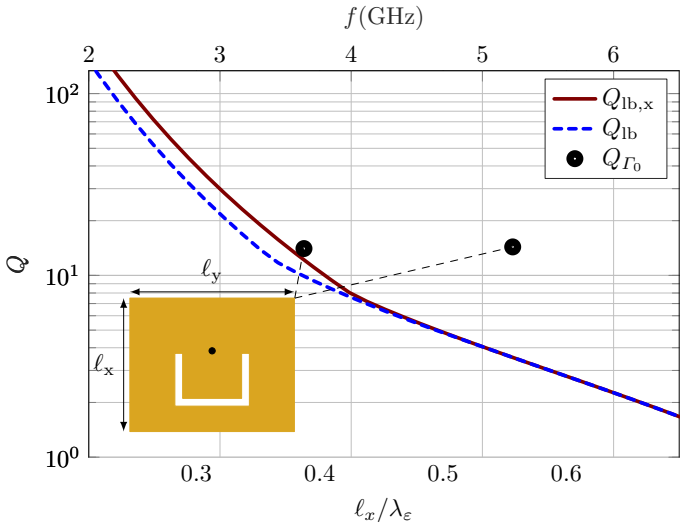

Figure 10: Lower Q-factor bounds for a design region with dimensions $\ell_{\mathrm{x}} = 21.5\,\mathrm{mm}$ and $\ell_{\mathrm{y}} = 26.5\,\mathrm{mm}$ compared with a dual resonant U-slot patch antenna design adapted from [19], where the relative permittivity is $\varepsilon_{\mathrm{r}} = 2.2$ and substrate thickness is $h = 4.5\,\mathrm{mm}$.

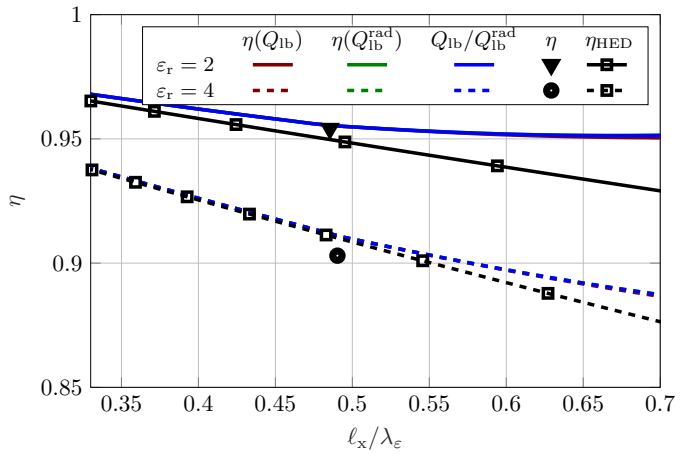

Figure 11: Radiation efficiency due to surface-wave losses of lower Q-factor bounds currents for the lossless case given a patch with dimensions $\ell_y = 0.77\ell_x$ and dielectric thickness $h = 0.05\ell_x$. Two relative permittivities $\varepsilon_r \in \{2, 4\}$ are used and for half-wavelength resonant patches radiation efficiency calculated with FEKO are shown with markers. The approximate radiation efficiency for a HED (6.1) is also shown for both relative permittivities.

the presented range of $\ell_x/\lambda_\varepsilon$ for both relative permittivities there is no significant noticeable difference in radiation efficiency between Q_{lb} and Q_{rad}. Additionally, the quotient Q_{lb}/Q_{lb}^{rad} (see, (3.5)), indicating similar radiation efficiency, correctly suggests that the optimal currents effectively produce the same Q-factor. At the half-wavelength resonance FEKO simulations are used to compute the radiation efficiency as indicated with markers in Fig. 11. The FEKO simulations' radiation efficiency was determined by integrating over the far-field above the patch (radiated power) and comparing this with the input power. The small difference between FEKO and the bounds come from a combination of factors *e.g.*, a different feed model. Furthermore, it can clearly be seen that a greater relative permittivity and $\ell_x/\lambda_\varepsilon$ results in greater surface-wave losses when computing Q-factor bounds.

For a horizontal electric (Hertzian) dipole (HED) on the patch region, given a thin substrate, an approximate ratio between surface-wave power and radiated power is [30]

$$\frac{P_{sw}}{P_r} = \frac{3\pi^2}{2} \frac{(\varepsilon_r - 1)^3 \, h/\lambda}{\varepsilon_r^2 (\varepsilon_r - 1) + \frac{2}{5}\varepsilon_r}. \tag{6.1}$$

From this expression, radiation efficiency can, in a lossless case, be approximated as $\eta_{HED} = 1/(1 + P_{sw}/P_r)$. This has been shown to be accurate up to $h \leq 0.05\lambda$ [30].

In Fig. 11, the radiation efficiency obtained for an HED is shown with two black lines. These lines suggest that it can be sufficient to use (6.1) in determining radiation efficiency once bounds have been computed with (4.1).

7 Conclusion

In this paper, a formulation to compute lower Q-factor bounds for microstrip patch antennas is presented. The results are numerically validated against expressions available in literature for computing Q-factor from fractional bandwidth and input impedance. Current optimization is used to compute the lower Q-factor bounds. These bounds are shown to be tight for classic patch antenna designs. This further emphasizes the versatility of current optimization as a method of determining lower Q-factor bounds, previously generally only applied to antennas in free space. Further, the microstrip patch antennas under investigation serve as a canonical case for introducing the method.

It is shown that lower Q-factor bounds can be approximated by a simple method that only requires the simulation of half-wavelength resonant patch antennas. The low-frequency lower Q-factor bounds scale differently from those of antennas in free space, due to the ground plane. Further, this bound is orders of magnitude tighter than the Chu bound. Moreover, it shows that circular polarization cannot enhance bandwidth for the patch antennas considered here.

Some practical applications of the bounds are also considered, such as how the design frequency and design region impact the bounds for a given dielectric substrate. Obtained Q-factor for dual resonant antennas are also compared to the bounds for both orthogonal, and parallel polarization, of the two resonances. The bounds are computed with and without surface-wave losses, showing that for electrically thin substrates, the surface-wave contribution to the bounds is relatively small and can be accurately approximated by a closed form expression.

Among potential extensions of the proposed method are the addition of shorting pins, stacked patches and considering other design region shapes *e.g.*, circular. A further extension is using two resonances to widen the bandwidth.

Acknowledgment

This work was supported by the Swedish Research Council (2017-04656) and the Hedda Andersson guest professor program at Lund University.

Appendix A MoM impedance angular frequency derivative

The MoM impedance matrix in (2.3), assuming no ohmic losses, can be expressed as

$$\mathbf{Z} = \mathrm{j}\omega\mu_0\mathbf{L} + \frac{\mathbf{C}_\mathrm{i}}{\mathrm{j}\omega\varepsilon_0}, \tag{A.1}$$

where $\mathbf{L}$ and $\mathbf{C}_\mathrm{i}$ are broadly linked to the inductance and inverse of the capacitance, respectively. The permeability of free space is denoted μ_0, the permittivity of free space is denoted ε_0, and the speed of light in free space is given by $c_0 = 1/\sqrt{\varepsilon_0\mu_0}$.

Matrix $\mathbf{L}$ has elements

$$L_{mn} = \int_{\Omega}\int_{\Omega} \boldsymbol{\psi}_m(\boldsymbol{r}_1) \cdot \mathbf{G}_{\mathrm{A}} \cdot \boldsymbol{\psi}_n(\boldsymbol{r}_2)\, \mathrm{dS}_1\, \mathrm{dS}_2 \tag{A.2}$$

and matrix $\mathbf{C}_{\mathrm{i}}$ has elements

$$C_{imn} = \int_{\Omega}\int_{\Omega} \nabla_1 \cdot \boldsymbol{\psi}_m(\boldsymbol{r}_1) \nabla_2 \cdot \boldsymbol{\psi}_n(\boldsymbol{r}_2) \mathrm{G}_{\mathrm{V}}\, \mathrm{dS}_1\, \mathrm{dS}_2, \tag{A.3}$$

where the basis functions are denoted $\boldsymbol{\psi}_m$ and $\boldsymbol{\psi}_n$. Since all basis functions are assumed to be on the patch region, the distances between basis functions are equal to their radial distances, given by $\rho_{12} = |\boldsymbol{r}_1 - \boldsymbol{r}_2|$. The vector Green dyadic, $\mathbf{G}_{\mathrm{A}} = \mathrm{G}_{\mathrm{A}}(\hat{\boldsymbol{x}}\hat{\boldsymbol{x}} + \hat{\boldsymbol{y}}\hat{\boldsymbol{y}})$ can be calculated from the scalar, G_{A}, since no z-directed basis functions are assumed. Along with the scalar Green's function, G_{V}, are expressed in radial coordinates as

$$\mathrm{G}_{\mathrm{A}}\left(\rho_{12}\right) = \frac{1}{4\pi}\mathrm{S}_0\left(\frac{1}{D_{\mathrm{TE}}}\right) \quad \mathrm{G}_{\mathrm{V}}\left(\rho_{12}\right) = \frac{1}{4\pi}\mathrm{S}_0\left(\frac{N}{D_{\mathrm{TE}}D_{\mathrm{TM}}}\right), \tag{A.4}$$

where the Sommerfeld integral, S_0 is [31]

$$\mathrm{S}_0(g) = 2\int_0^{\infty} J_0\left(k_\rho \rho_{12}\right) k_\rho g\left(k_\rho, \omega\right) \mathrm{d}k_\rho, \tag{A.5}$$

where J_0 is the Bessel function of order 0 and k_ρ is the radial spectral coordinate. Further, D_{TE}, D_{TM}, and N are defined as [31]

$$\begin{aligned} D_{\mathrm{TE}} &= u_1 + u_2 \coth u_2 h \\ D_{\mathrm{TM}} &= \varepsilon_{\mathrm{r}} u_1 + u_2 \tanh u_2 h \\ N &= u_1 + u_2 \tanh u_2 h, \end{aligned} \tag{A.6}$$

with

$$u_1 = \sqrt{k_\rho^2 - \omega^2 c_0^{-2}} \quad \text{and } u_2 = \sqrt{k_\rho^2 - \omega^2 \varepsilon_{\mathrm{r}} c_0^{-2}}. \tag{A.7}$$

The following derivation is used to compute stored energies (3.8). Firstly, the angular frequency derivative of the MoM impedance matrix is computed as

$$\frac{\partial \mathbf{Z}}{\partial \omega} = \mathrm{j}\mu_0 \mathbf{L} + \mathrm{j}\mathbf{C}_{\mathrm{i}} \frac{1}{\omega^2 \varepsilon_0} + \mathrm{j}\omega\mu_0 \frac{\partial \mathbf{L}}{\partial \omega} + \frac{1}{\mathrm{j}\omega\varepsilon_0} \frac{\partial \mathbf{C}_{\mathrm{i}}}{\partial \omega}, \tag{A.8}$$

and the imaginary part can easily be separated for computations of (3.8). The angular frequency derivative of $\mathbf{L}$ is

$$\frac{\partial L_{\mathrm{mn}}}{\partial \omega} = \int_{\Omega}\int_{\Omega} \boldsymbol{\psi}_m(\boldsymbol{r}_1) \cdot \boldsymbol{\psi}_n(\boldsymbol{r}_2) \frac{\partial \mathrm{G}_{\mathrm{A}}}{\partial \omega}\, \mathrm{dS}_1\, \mathrm{dS}_2 \tag{A.9}$$

and the angular frequency derivative of $\mathbf{C}_{\mathrm{i}}$ is

$$\frac{\partial C_{imn}}{\partial \omega} = \int_{\Omega}\int_{\Omega} \nabla_1 \cdot \boldsymbol{\psi}_m(\boldsymbol{r}_1) \nabla_2 \cdot \boldsymbol{\psi}_n(\boldsymbol{r}_2) \frac{\partial \mathrm{G}_{\mathrm{V}}}{\partial \omega}\, \mathrm{dS}_1\, \mathrm{dS}_2. \tag{A.10}$$

To calculate angular frequency derivatives of the vector and scalar Green's functions in (A.4), differentiation is moved inside the integral in the Sommerfeld integral under conditions given by Lebesgue's dominated convergence theorem [40]. The angular frequency derivative of the vector Green's function can then be written as

$$\frac{\partial}{\partial\omega}\mathrm{G_A}\left(\rho_{12}\right)=\frac{1}{4\pi}\mathrm{S}_0\left(\frac{\partial}{\partial\omega}\frac{1}{D_{\mathrm{TE}}}\right). \tag{A.11}$$

The final expressions follow from basic differentiation rules and explicit differentiation of terms in (A.4). The angular frequency derivative of D_{TE}^{-1} is given by

$$\frac{\partial}{\partial\omega}\frac{1}{D_{\mathrm{TE}}}=-\frac{\frac{\partial}{\partial\omega}D_{\mathrm{TE}}}{D_{\mathrm{TE}}^2}, \tag{A.12}$$

where

$$\frac{\partial D_{\mathrm{TE}}}{\partial\omega}=\frac{\omega}{c_0^2}\left(\varepsilon_{\mathrm{r}}h\,\mathrm{csch}^2\,hu_2-\frac{1}{u_1}-\frac{\varepsilon_{\mathrm{r}}\coth hu_2}{u_2}\right). \tag{A.13}$$

The angular frequency derivative of the scalar Green's function (A.4) is expressed as

$$\frac{\partial}{\partial\omega}\mathrm{G_V}\left(\rho_{12}\right)=\frac{1}{4\pi}\mathrm{S}_0\left(\frac{\partial}{\partial\omega}\frac{N}{D_{\mathrm{TE}}D_{\mathrm{TM}}}\right), \tag{A.14}$$

which is further computed using

$$\frac{\partial}{\partial\omega}\frac{N}{D_{\mathrm{TE}}D_{\mathrm{TM}}}=\frac{D_{\mathrm{TE}}D_{\mathrm{TM}}\left(\frac{\partial N}{\partial\omega}\right)-N\left(\frac{\partial D_{\mathrm{TE}}D_{\mathrm{TM}}}{\partial\omega}\right)}{\left(D_{\mathrm{TE}}D_{\mathrm{TM}}\right)^2}, \tag{A.15}$$

where

$$\frac{\partial}{\partial\omega}D_{\mathrm{TE}}D_{\mathrm{TM}}=D_{\mathrm{TM}}\frac{\partial}{\partial\omega}D_{\mathrm{TE}}+D_{\mathrm{TE}}\frac{\partial}{\partial\omega}D_{\mathrm{TM}}, \tag{A.16}$$

with

$$\frac{\partial D_{\mathrm{TM}}}{\partial\omega}=\frac{\omega\varepsilon_{\mathrm{r}}}{c_0^2}\left(-\frac{1}{u_1}-\frac{\tanh hu_2}{u_2}-h\,\mathrm{sech}^2\,hu_2\right) \tag{A.17}$$

and

$$\frac{\partial N}{\partial\omega}=\frac{\omega}{c_0^2}\left(-\frac{1}{u_1}-\frac{\varepsilon_{\mathrm{r}}\tanh hu_2}{u_2}-\varepsilon_{\mathrm{r}}h\,\mathrm{sech}^2\,hu_2\right). \tag{A.18}$$

The Sommerfeld integrals of (A.11) and (A.14) can be solved in the spectral-domain by going out into the complex plane to avoid the singularity and discontinuity at $u_1=0$. For (A.14) the singularity of the first transverse magnetic surface wave mode at $D_{\mathrm{TM}}=0$ should also be avoided. It is assumed there is only one surface wave mode. Note, there is no singularity or discontinuity at $u_2=0$ [31]. To integrate the tail, partition-extrapolation using the Mosig–Michalski algorithm [28] can be used, except when $\rho_{12}=0$, where the integrals are non-oscillatory as a result of $J_0(0)=1$ in (A.6). These integrals are also finite and relatively easy to solve.

From Sommerfeld integrals an asymptotic expression for the radiated far field can be derived [31]. Given radiation in the z-direction from an HED at the origin,

the far-field can be rewritten assuming for instance an x-directed current producing an $\hat{\boldsymbol{x}}$-polarized far-field at $x = 0$, $y = 0$ and $z \to \infty$.

Using the far-field relation [10], $\boldsymbol{E}_{\hat{\boldsymbol{e}}}(\hat{\boldsymbol{r}}) = \mathrm{e}^{-\mathrm{j}kr}\boldsymbol{F}_{\hat{\boldsymbol{e}}}(\hat{\boldsymbol{r}})/r$ as $r \to \infty$, and the current density expanded in local basis functions as (2.1), the far-field vector can then be expressed as

$$\boldsymbol{F}_{\hat{\boldsymbol{e}}}(\hat{\boldsymbol{z}}) \approx \mathbf{FI} = \sum_{m=1}^{M} \frac{-\mathrm{j}\omega\mu_0 I_m}{2\pi\big(1 - \mathrm{j}\sqrt{\varepsilon_r}\cot(kh\sqrt{\varepsilon_r})\big)} \int_{\Omega} \hat{\boldsymbol{e}}^* \cdot \boldsymbol{\psi}_m(\boldsymbol{r})\mathrm{e}^{\mathrm{j}k\hat{\boldsymbol{z}}\cdot\boldsymbol{r}}\,\mathrm{dS}, \tag{A.19}$$

where $\hat{\boldsymbol{e}}$ is the unit polarization vector and superscript * denotes the complex conjugate.

Appendix B Low-frequency expansion

Mirror currents are used to determine the low-frequency expansion for horizontal current densities in a region Ω at height h above an infinite PEC ground plane. The electric far-field $\boldsymbol{F}$ in a direction $\hat{\boldsymbol{r}}$ from a current density $\boldsymbol{J}$ in free space can be expressed as

$$\boldsymbol{F}(\hat{\boldsymbol{r}}) = \frac{-\mathrm{j}k\eta_0}{4\pi}\left(\hat{\boldsymbol{r}} \times \int_{\mathbb{R}^3} \mathrm{e}^{\mathrm{j}k\hat{\boldsymbol{r}}\cdot\boldsymbol{r}_1}\boldsymbol{J}(\boldsymbol{r}_1)\,\mathrm{dV}_1\right) \times \hat{\boldsymbol{r}} \tag{B.1}$$

which for the patch geometry with surface currents and surface mirror currents reduces to

$$\begin{aligned}\int_{\mathbb{R}^3} \mathrm{e}^{\mathrm{j}k\hat{\boldsymbol{r}}\cdot\boldsymbol{r}_1}\boldsymbol{J}(\boldsymbol{r}_1)\,\mathrm{dV}_1 &= \int_{\Omega} \mathrm{e}^{\mathrm{j}k\hat{\boldsymbol{r}}\cdot\boldsymbol{r}_1}\boldsymbol{J}_{\mathrm{s}}(\boldsymbol{r}_1) - \mathrm{e}^{\mathrm{j}k\hat{\boldsymbol{r}}\cdot(\boldsymbol{r}_1 - 2\hat{\boldsymbol{z}}\boldsymbol{r}_1\cdot\hat{\boldsymbol{z}})}\boldsymbol{J}_{\mathrm{s}}(\boldsymbol{r}_1)\,\mathrm{dS}_1 \\ &= \int_{\Omega} \left(\mathrm{e}^{\mathrm{j}k\hat{\boldsymbol{r}}\cdot\boldsymbol{r}_1} - \mathrm{e}^{\mathrm{j}k\hat{\boldsymbol{r}}\cdot(\boldsymbol{r}_1 - 2h\hat{\boldsymbol{z}})}\right)\boldsymbol{J}_{\mathrm{s}}(\boldsymbol{r}_1)\,\mathrm{dS}_1 = \left(1 - \mathrm{e}^{-\mathrm{j}2hk\hat{\boldsymbol{r}}\cdot\hat{\boldsymbol{z}}}\right)\int_{\Omega} \mathrm{e}^{\mathrm{j}k\hat{\boldsymbol{r}}\cdot\boldsymbol{r}_1}\boldsymbol{J}_{\mathrm{s}}(\boldsymbol{r}_1)\,\mathrm{dS}_1\end{aligned} \tag{B.2}$$

The low-frequency expansion [26] is expressed in the electric $\boldsymbol{p}$ and magnetic $\boldsymbol{m}$ dipole moments determined from the surface charge ϱ_{s} and surface current $\boldsymbol{J}_{\mathrm{s}}$ densities in Ω, i.e.

$$\boldsymbol{F}(\hat{\boldsymbol{r}}) \approx \mathrm{j}2hk\hat{\boldsymbol{r}}\cdot\hat{\boldsymbol{z}}\frac{k^2}{4\pi\varepsilon_0}\left(\hat{\boldsymbol{r}} \times (\boldsymbol{p} \times \hat{\boldsymbol{r}}) + c_0^{-1}\boldsymbol{m} \times \hat{\boldsymbol{r}}\right) \tag{B.3}$$

as $k \to 0$, where

$$\boldsymbol{p} = \int_{\Omega} \boldsymbol{r}\varrho_{\mathrm{s}}(\boldsymbol{r})\,\mathrm{dS} \quad \text{and } \boldsymbol{m} = \frac{1}{2}\int_{\Omega} \boldsymbol{r} \times \boldsymbol{J}_{\mathrm{s}}(\boldsymbol{r})\,\mathrm{dS} \tag{B.4}$$

and it is assumed that the total charge in region Ω is zero. The radiated power for the patch geometry scales as k^6 in the electrically small limit in contrast to k^4 for an electrically small antenna in free space [6, 11]. The corresponding stored energy is independent of k in the limit $k \to 0$ and approaches the static energy. This produces a Q-factor scaling from (3.3)

$$Q \sim k^{-5} \sim \lambda^5 \tag{B.5}$$

in contrast to $Q \geq (ka)^{-3}$ for a spherical region with radius a in free space [6] and $Q \geq 6\pi/(\gamma k^3)$ for electric dipole radiators in an arbitrary shaped region with high-contrast polarizability γ [11].

If the height (h) is made proportional to the wavelength in free space $h \sim \lambda$, this from (B.3) produces radiated power scaling of k^4.

References

[1] (2022) CST Studio Suite 3D EM simulation and analysis software.

[2] (2022) FEKO. Altair.

[3] A. Beck and Y. C. Eldar. "Strong duality in nonconvex quadratic optimization with two quadratic constraints". *SIAM Journal on Optimization* 17 (3) (2006): pp. 844–860.

[4] S. P. Boyd and L. Vandenberghe. "Convex Optimization". Cambridge Univ. Pr., 2004.

[5] M. Capek, M. Gustafsson, and K. Schab. "Minimization of antenna quality factor". *IEEE Trans. Antennas Propag.* 65 (8) (2017): pp. 4115–4123.

[6] L. J. Chu. "Physical limitations of omni-directional antennas". *J. Appl. Phys.* 19 (1948): pp. 1163–1175.

[7] A. G. Derneryd. "Analysis of the microstrip disk antenna element". *IEEE Trans. Antennas Propag.* 27 (5) (1979): pp. 660–664.

[8] R. Garg, P. Bhartia, I. Bahl, and A. Ittipiboon. "Microstrip Antenna Design Handbook". Artech House, 2001.

[9] M. Gustafsson and M. Capek. "Maximum gain, effective area, and directivity". *IEEE Trans. Antennas Propag.* 67 (8) (2019): pp. 5282–5293.

[10] M. Gustafsson and S. Nordebo. "Optimal antenna currents for Q, superdirectivity, and radiation patterns using convex optimization". *IEEE Trans. Antennas Propag.* 61 (3) (2013): pp. 1109–1118.

[11] M. Gustafsson, C. Sohl, and G. Kristensson. "Physical limitations on antennas of arbitrary shape". *Proc. R. Soc. A* 463 (2007): pp. 2589–2607.

[12] M. Gustafsson, D. Tayli, C. Ehrenborg, M. Cismasu, and S. Nordebo. "Antenna current optimization using MATLAB and CVX". *FERMAT* 15 (5) (2016): pp. 1–29.

[13] M. Gustafsson, M. Capek, and K. Schab. "Tradeoff between antenna efficiency and Q-factor". *IEEE Trans. Antennas Propag.* 67 (4) (2019): pp. 2482–2493.

[14] M. Gustafsson and C. Ehrenborg. "State-space models and stored electromagnetic energy for antennas in dispersive and heterogeneous media". *Radio Sci.* 52 (2017).

[15] M. Gustafsson, K. Schab, L. Jelinek, and M. Capek. "Upper bounds on absorption and scattering". *New Journal of Physics* 22 (073013) (2020).

[16] R. F. Harrington. "Time Harmonic Electromagnetic Fields". McGraw-Hill, 1961.

[17] R. F. Harrington. "Field Computation by Moment Methods". Macmillan, 1968.

[18] R. F. Harrington and J. R. Mautz. "Control of radar scattering by reactive loading". *IEEE Trans. Antennas Propag.* 20 (4) (1972): pp. 446–454.

[19] M. N. Hasan, S. W. Shah, M. I. Babar, and Z. Sabir. "Design and simulation based studies of a dual band u-slot patch antenna for wlan application". In: *2012 14th International Conference on Advanced Communication Technology (ICACT)*. 2012, pp. 997–1001.

[20] R. L. Haupt and D. H. Werner. "Genetic Algorithms in Electromagnetics". Wiley-IEEE Press, 2007.

[21] T. Huynh and K.-F. Lee. "Single-layer single-patch wideband microstrip antenna". *Electronics Letters* 31 (1995): pp. 1310–1312.

[22] J. R. James and P. S. Hall. "Handbook of microstrip antennas". English. Peregrinus on behalf of the Institution of Electrical Engineers London, U.K, 1989, 2 v. (xxiii, 1312 p.) :

[23] J. R. James, P. S. Hall, and C. Wood. "Microstrip antenna : theory and design". English. Peregrinus on behalf of the Institution of Electrical Engineers London ; New York, 1981, x, 290 p. :

[24] L Jelinek and M Capek. "Optimal currents on arbitrarily shaped surfaces". *IEEE Trans. Antennas Propag.* 65 (1) (2017): pp. 329–341.

[25] B. L. G. Jonsson, S. Shi, L. Wang, F. Ferrero, and L. Lizzi. "On methods to determine bounds on the Q-factor for a given directivity". *IEEE Trans. Antennas Propag.* 65 (11) (2017): pp. 5686–5696.

[26] G. Kristensson. "Scattering of Electromagnetic Waves by Obstacles". SciTech Publishing, an imprint of the IET, 2016.

[27] D.-H. Kwon and D. M. Pozar. "Spectral-domain radiation Q analysis of a planar dipole over a conducting ground plane". In: *2015 IEEE International Symposium on Antennas and Propagation USNC/URSI National Radio Science Meeting*. 2015, pp. 1404–1405.

[28] K. A. Michalski and J. R. Mosig. "Efficient computation of sommerfeld integral tails – methods and algorithms". *Journal of Electromagnetic Waves and Applications* 30 (3) (2016): pp. 281–317.

[29] J. R. Mosig. "Integral equation techniques for 3D microstrip structures". *Review of Radio Science* (1993): pp. 127–153.

[30] J. R. Mosig, R. C. Hall, and F. E. Gardiol. "Numerical analysis of microstrip patch antennas". In: *Handbook of Microstrip Antennas*. Ed. by J. R. James and P. S. Hall. London: Peregrinus, 1989, pp. 391–453.

[31] J. R. Mosig and F. E. Gardiol. "A dynamical radiation model for microstrip structures". In: *Advances in Electronics and Electron Physics*. Ed. by P. W. Hawkes. Vol. 59. Academic Press, 1982, pp. 139 –237.

[0] B. A. Nel, A. K. Skrivervik, and M. Gustafsson. "Q-factor bounds for microstrip patch antennas". *IEEE Transactions on Antennas and Propagation* (2023).

[32] V. Palanisamy and R. Garg. "Rectangular ring and H-shaped microstrip antennas Alternatives to rectangular patch antenna". *Electronics Letters* 21 (1985): pp. 874–876.

[33] D. M. Pozar. "Microstrip antenna". *Proc. IEEE* 80 (1) (1992): pp. 79–91.

[34] D. M. Pozar. "New results for minimum Q, maximum gain, and polarization properties of electrically small arbitrary antennas". In: *Antennas and Propagation, 2009. EuCAP 2009. 3rd European Conference on*. 2009, pp. 1993–1996.

[35] Y. Rahmat-Samii and E. Michielssen. "Electromagnetic Optimization by Genetic Algorithms". Wiley Series in Microwave and Optical Engineering. John Wiley & Sons, 1999.

[36] K. Schab, L. Jelinek, M. Capek, C. Ehrenborg, D. Tayli, G. A. Vandenbosch, and M. Gustafsson. "Energy stored by radiating systems". *IEEE Access* 6 (2018): pp. 10553 –10568.

[37] A. Skrivervik, J.-F. Zurcher, O. Staub, and J. Mosig. "PCS antenna design: the challenge of miniaturization". *IEEE Antennas and Propagation Magazine* 43 (4) (2001): pp. 12–27.

[38] A. Sommerfeld. "Über die ausbreitung der wellen in der drahtlosen telegraphie". *Annalen der Physik* 333 (1909): pp. 665–736.

[39] J.-E. Sten, A Hujanen, and P. Koivisto. "Quality factor of an electrically small antenna radiating close to a conducting plane". *IEEE Trans. Antennas Propag.* 49 (5) (2001): pp. 829–837.

[40] E. Talvila. "Necessary and sufficient conditions for differentiating under the integral sign". *The American Mathematical Monthly* 108 (6) (2001): pp. 544–548.

[41] D. Tayli and M. Gustafsson. "Physical bounds for antennas above a ground plane". *IEEE Antennas Wireless Propag. Lett.* 15 (2016): pp. 1281–1284.

[42] G. A. E. Vandenbosch. "Reactive energies, impedance, and Q factor of radiating structures". *IEEE Trans. Antennas Propag.* 58 (4) (2010): pp. 1112–1127.

[43] A. D. Yaghjian and S. R. Best. "Impedance, bandwidth, and Q of antennas". *IEEE Trans. Antennas Propag.* 53 (4) (2005): pp. 1298–1324.

[44] J.-F. Zürcher and F. E. Gardiol. "Broadband Patch Antennas". Artech House, 1995.